

Efficiency Optimization with a Novel Magnetic-Circuit Model for Inductive Power Transfer in EVs

Yunyu Tang^{*}, Fan Zhu^{*}, and Hao Ma[†]

^{*,†}College of Electrical Engineering, Zhejiang University, Hangzhou, China

Abstract

The technology of inductive power transfer has been proved to be a promising solution in many applications especially in electric vehicle (EV) charging systems, due to its features of safety and convenience. However, loosely coupled transformers lead to the system efficiency not coming up to the expectation at the present time. Therefore, at first, the magnetic core losses are calculated with a novel magnetic-circuit model instead of the commonly used finite-element-method (FEM) simulations. The parameters in the model can be obtained with a one-time FEM simulation, which makes the calculation process expeditious. When compared with traditional methods, the model proposed in the paper is much less time-consuming and relatively accurate. These merits have been verified by experimental results. Furthermore, with the proposed loss calculation model, the system is optimized by parameter sweeping, such as the operating frequency and winding turns. Specifically, rather than a predesigned switching frequency, a more efficiency-optimized frequency for the series-parallel (SP) compensation topology is detected and a detailed investigation has been presented accordingly. The optimized system is capable of an efficiency that is greater than 93% at a coil separation distance of 200mm and coil dimensions of 600mm×400mm.

Key words: Core losses, Efficiency, Inductive power transfer, Loosely coupled transformer, Magnetic-circuit model

I. INTRODUCTION

Recently, more attention has been paid to inductive power transfer since this technology provides a safer and more convenient way to charge batteries when compared with traditional contact methods. Based on the principle of magnetic induction, many applications have been developed, including biomedical implants [1], lighting systems [2] factory applications [3] and electric vehicles (EVs) [4]-[7].

For stationary inductive charging systems [8]-[12], the arrangement of the windings and magnetic cores in the lumped loosely coupled transformers is the key that determines the system efficiency. Generally, a high efficiency can be achieved by a comprehensive loss analysis. For most power electronics circuits, an analysis of all the partial losses including switching device losses, winding losses and

magnetic core losses has been developed on a large scale [13]-[15]. However, for inductive charging system, the losses in the magnetic cores and windings should be investigated specifically. For the magnetic cores, the plane transformer structure results in a flux density distribution that is not uniform, which makes it impossible to directly employ the Steinmetz Equation [16] to calculate the core losses. Alternatively, FEM simulation tools like ANSYS and JMAG are widely implemented to obtain the core loss distributions [17], [18]. However, these methods are very time-consuming for different current excitations and coil turns, especially when 3D transformer models are elaborately meshed and calculated for loosely coupled transformer structures. The lumped magnetic circuit is an alternative tool for calculating flux density [19]-[21]. In view of this, a magnetic-circuit model is proposed according to the features of the solenoid structure and its corresponding simulated flux distributions. The magnetic reluctance can be derived by one-time FEM simulation results.

For a system with a limited space and cost, the switching frequency and turn combinations are essential parameters for

Manuscript received Apr. 26, 2017; accepted Sep. 24, 2017.

Recommended for publication by Associate Editor M. Vilathgamuwa.

[†]Corresponding Author: mahao@zju.edu.cn

Tel: +0571-87572503, Zhejiang University

^{*}College of Electrical Engineering, Zhejiang University, China

efficiency optimization. Consequently, a mathematical model is built to provide a simple and fast method for different current conditions and winding turns. Windings are usually made of Litz wires to achieve excellent performance in high-frequency and high-power applications. In order to obtain the winding losses, there are two main ways: analytical calculation models [22], [23] and measurement methods [24]-[26]. Analytical models have not been proved to be suitable for loosely coupled transformers due to the number of strands in the Litz wires. In addition, the leakage inductance make the calculation much more complicated and impractical. In this paper, the winding resistance is derived based on the measurement method proposed in [25].

Normally, an optimized system can be obtained by sweeping the parameters [27]-[31]. For a designed system, the dimensions of the transformers are restricted by the cost and the available space for installation. As a result, parameters such as the switching frequency and the primary and secondary turns play critical roles in the optimization process. However, the sweeps may take a lot of time with the FEM loss calculation method. Hence, the optimization process was carried out based on the proposed loss calculation methods in this paper. For the SP compensation topology, the switching frequency is usually determined as the resonant frequency of the compensation network. However, a higher-efficiency frequency was detected with the proposed parameter sweeps. In addition, a selection map of the coil turn combinations was investigated to find the optimized winding turns. Specifically, the pattern of the map varies with the switching frequency.

In this paper, the structure optimization of solenoid transformers was carried. Then, based on the magnetic flux distribution and electromagnetic theory, an equivalent magnetic-circuit model was built and a corresponding transformer model was derived. Subsequently, the winding resistance was obtained by a simple measurement method. After that, the losses were measured and compared with the calculated results. Due to the proposed method, the parameters sweep was carried out to find the conditions for higher efficiency. A higher-efficiency frequency and a map for choosing the coil turns were presented and the corresponding experiment shows great agreement with the proposed model.

II. TRANSFORMER STRUCTURE

As discussed in [10], there are two main magnetic structures that are widely implemented in inductive power transfer systems. These structures are single-sided structures [8]-[10] with the flux mainly flowing on one side of the pad, and double-sided structures with two-sided flux patterns [11], [12]. For EV applications, the distance between the primary and secondary plates can be as much as 200mm, which makes

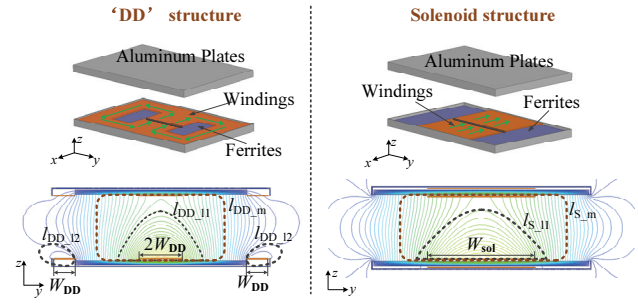


Fig. 1. Simulation models of the 'DD' and solenoid structures, and a comparison of their flux path distributions.

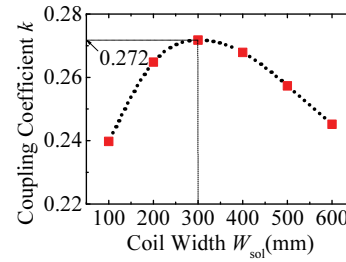


Fig. 2. Coupling coefficient versus coil width for solenoid structures.

TABLE I
DIMENSIONS OF THE SIMULATION MODEL IN FIGURE 1

Length of the plate (y axis)	600mm
Width of the plate (x axis)	400mm
Length of ferrite (y axis)	595mm
Length of ferrite (x axis)	395mm
Gap between the plates (z axis)	200mm
Thickness of the cores	12mm
Thickness of the windings	3mm
Thickness of the aluminum plates	3mm

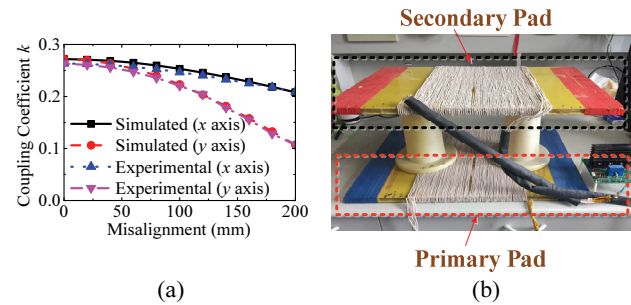


Fig. 3. Solenoid pads: (a) coupling coefficient versus misalignment between the primary and secondary plates; (b) picture of the pads.

the 'DD' structure more suitable than the circular structure since the magnetic flux radius of the former is larger than that of the latter with the same dimensions [11]. Another structure includes the double-sided structures, such as solenoid or pipe [11]-[12]. In order to eliminate the back leakage flux, aluminum plates are usually employed.

The 'DD' and solenoid structures are compared in view of the flux distribution, as shown in Fig. 1. The black shaded part across the windings is the area for injecting current excitations for the FEM simulation. The 'DD' structure is represented with two current circles and the solenoid structure is depicted with one current circle. It should be noted that the main reason for a low coupling is that the mutual inductance is much lower than the coils' self-inductance. As illustrated in Fig. 1, the mutual flux is influenced by the outside mutual flux paths I_{DD_m} and I_{s_m} . Meanwhile, the internal leakage flux paths I_{DD_l1} and I_{s_l1} as well as the outside leakage paths I_{DD_l2} affect the leakage flux. As discussed in [11], the solenoid structure can perform better coupling with a proper design, due to the nature of magnetic fields. Therefore, the solenoid structure is implemented as the study case in this paper.

As can be seen from Fig. 1, the width of the winding W_{sol} is one of the key parameters that determines the coupling performance. Hence, as plotted in Fig. 2, the coupling performance of the solenoid pads was simulated with different winding widths for the fixed dimensions of the plates. The relative permeability of the DMR47 ferrites is 2500. The dimension specifications of the built structures are shown in Table I. According to the simulated results in Fig. 2, the best coupling performance occurs when the coil width of the solenoid structure is 300mm.

When there is a misalignment between the primary and secondary plates, the coupling may become worse. Thus, the coupling of the solenoid pads, when misaligned along x and y directions, is compared as exhibited in Fig. 3(a). To verify the simulation results through FEM simulations, the transformers of the solenoid structure were fabricated with the dimensions in Table I and shown in Fig. 3(b).

The windings are made of Litz wires and the magnetic cores are composed of ferrite bars. The obtained experimental results match well with the simulated results as depicted in Fig. 3(a). The results reveal that the coupling of the solenoid pads decreases inconspicuously along x direction but dramatically along y direction. It is worth noting that a higher coupling coefficient contributes to an increase in system efficiency increased and a reduction in the EMI problem.

III. A NOVEL MAGNETIC-CIRCUIT MODEL FOR SOLENOID STRUCTURES

For loosely coupled transformers, the core losses account for a significant component of the total losses. Therefore, it is necessary to model the core losses under different excitations to derive an optimized system. The most common method for doing this is adopting FEM simulation tools like ANSYS or JMAG to model the built transformers. However, when doing optimization with simulation tools, a lot of time may be consumed to obtain the losses under different working conditions due to the complex 3D models. Furthermore,

traditional loss calculation methods are not practical in this application owing to the non-uniform magnetic flux density in the magnetic cores. As demonstrated in [19]-[21], magnetic-circuit models are powerful tools for calculating flux density under different primary and secondary currents through the windings. In view of this, a novel magnetic-circuit model is proposed to calculate the magnetic flux distributions in magnetic cores. A one-time simulation is needed to derive the magnetic reluctance in the proposed circuit. The detailed steps are as follows:

Step 1: Sorting flux distribution

According to the simulated flux distribution surrounding the transformers in Fig. 4, the total flux is divided into three different parts: the internal leakage flux, the external leakage flux and the mutual flux. The internal leakage flux comprises the majority of the leakage flux since the path length of this part is much shorter than that of the other parts. In addition, aluminum plates are usually used to eliminate the leakage flux at the back side of pads. According to the simulation results in Fig. 4, most of the leakage flux inside the shielding plates is eliminated. Thus, only the external leakage flux is considered in the proposed model.

Step 2: Modeling the flux density distribution in the x - y plane

In the x - y plane, it can be found that the main flux density difference happens along the y axis. The proposed magnetic-circuit model is mainly used to illustrate the flux density distribution in the y - z plane. In order to simplify the 3D distribution into a 2D model and to make the proposed model more practical and accurate, a slight change of the flux density along the x axis is modeled with a total flux density array, which is calculated from the proposed magnetic-circuit model, and a coefficient matrix \mathbf{M} .

The flux density is uneven in different position of the transformer cores. Therefore, it is divided into several parts as shown in Fig. 5. The divided number can be determined according to the complexity of the model and the accuracy of the results. In each block, the flux density is treated as a homogeneous distribution. At first, the flux density along the x axis in the same column was summed in a different y axis as expressed with $[B_5, B_4, B_3, B_2, B_1, \dots]$. The total flux density array is an assumed variable quantity to represent the obvious flux variations along the y axis. The flux density in different blocks can be calculated by multiplying the coefficient matrix \mathbf{M} as $[m_{1,5}, m_{1,4}, m_{1,3}, m_{1,2}, m_{1,1}, \dots; m_{2,5}, \dots]$ with the total flux density along the y direction. For example, in Fig. 5, the flux density in the right column can be calculated with the total flux density B_5 and the corresponding coefficient column in the matrix \mathbf{M} , as given by:

$$[B_{1,5} \ B_{2,5} \ B_{3,5} \ B_{4,5} \ B_{1,5}] = B_5 \times [m_{1,5} \ m_{2,5} \ m_{3,5} \ m_{4,5} \ m_{1,5}] \quad (1)$$

The parameters in the flux-distribution matrix can be obtained by deriving the simulated results from a one-time

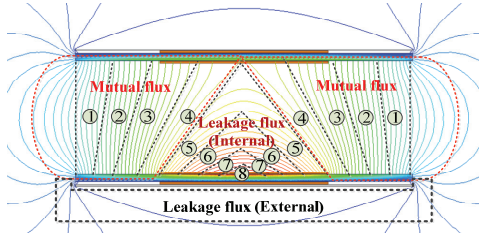


Fig. 4. Flux distribution of a solenoid structure and its corresponding sorted parts.

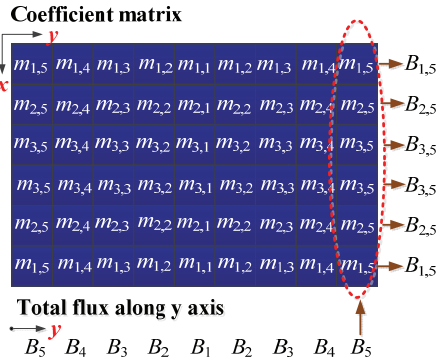


Fig. 5. Flux density distribution and coefficient for each of the divided cores versus the total flux density in each column.

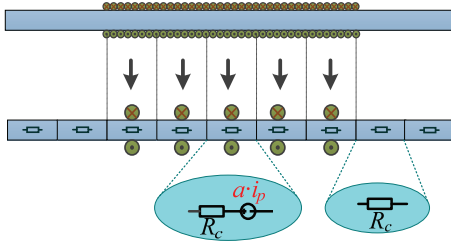


Fig. 6. 2D model of transformers and their equivalent MMF and magnetic reluctance.

FEM simulation. Obviously, increasing the number of divided parts can lead to more accurate loss results. However, the complexity of the modeling and calculation need to be considered.

Step 3. Building the magnetic-circuit model in the y-z plane

In the y-z plane, cores covered by windings can be treated as a magnetic motive force (MMF) (treated as a voltage source in a magnetic-circuit model) in series with a magnetic reluctance R_c , and the cores without being covered by windings can be modeled with a magnetic reluctance R_c , as depicted in Fig. 6. With different turns and current excitations in the windings, the corresponding MMFs can be easily obtained. In Fig. 6, i_p is the primary peak current and α is the coefficient that indicates the ratio of the divided MMF to i_p , which is related to the coil turns. The flux density is determined by the values of the reluctance including that inside the cores and in the air. The aim of the calculated model is to acquire the flux density in different parts of the

cores. Therefore, a lumped magnetic reluctance can be used to simplify the calculations. In addition, the small difference in the flux density along the z axis in the ferrite is not considered in the model, since the thickness of the ferrite is smaller when compared with the length and width of the designed pads. The non-uniform flux distribution in the air can be derived by lumped magnetic reluctances for the sake of simplicity.

On the basis of the flux distribution in Fig. 4, there are two main different interactive flux paths as shown in Fig. 7. The internal flux in Fig. 7(a) is mainly determined by the internal leakage reluctance above and below the windings, which can be merged by paralleling these two reluctance. The merged reluctance can be derived by the simulated fluxes Φ_1 and Φ_2 . Other main parts are the mutual flux and the back leakage flux, which are influenced by each other. Fig. 7(b) shows a magnetic model to model this part. The reluctance R_{m1} can be deduced by Kirchhoff's voltage law with the simulated fluxes Φ_1 , Φ_2 , Φ_3 , Φ_4 , Φ_{r1} and Φ_{r2} . Particularly, the separation number of the upper mutual flux is determined by the simulated flux distribution shown in Fig. 4. As can be seen from Fig. 4, the mutual flux is separated into areas 1 to 4, while the internal leakage flux is separated into areas 5 to 8, according to the flux distribution shown in the background flux lines. The separated number of the upper reluctance in the same area is determined by estimating the length of the corresponding parts in the magnetic cores. In this application, the divided number of the primary and secondary cores is 15 to satisfy the calculation accuracy. Fig. 8 shows the whole magnetic-circuit model by combining Fig. 6, Fig. 7 and areas 1 to 8 in Fig. 4. As discussed in Section II, the best coupling performance can be acquired with a 300mm coil width. Hence, the covered winding width in Fig. 8 is fixed at half of the total length. The MMFs are divided into 9 uniform parts and the magnetic reluctance in the internal flux, the external flux and the mutual flux are composed of 12 parts as $\{R_{l1}, R_{l2}, R_{l3}, R_{l4}\}$, $\{R_{l5}, R_{l6}, R_{l7}, R_{l8}\}$ and $\{R_{m1}, R_{m2}, R_{m3}, R_{m4}\}$, respectively. It should be noted that the magnetic-circuit model is forced by a single-sided magnetic force. The total flux density inside the magnetic cores can be obtained by adding the flux density forced by the secondary MMFs.

Step 4: Deriving the parameters in the proposed model

In contrast to traditional transformers, the values of $\{R_{l1}, R_{l2}, R_{l3}, R_{l4}\}$, $\{R_{l5}, R_{l6}, R_{l7}, R_{l8}\}$ and $\{R_{m1}, R_{m2}, R_{m3}, R_{m4}\}$ cannot be derived with empirical equations, since the flux distribution around the pads is not uniform. In order to derive these parameters, a one-time FEM simulation was carried out to get the flux distributions of Φ_1 to Φ_{12} . By substituting these flux values into the model in Fig. 8, the magnetic reluctance can be derived according to Kirchhoff's Law. The detailed deriving process is shown as follows.

As can be seen in Fig. 8, the cores in the y direction are divided into 15 parts. If the discretization number is too small,

the difference in the flux distribution along the y axis cannot be depicted precisely. Otherwise, too large a number can result in a complicated model, which is not desirable for the optimization process. Thus, the discretization number is 15 as a tradeoff between precision and complexity. Specifically, the windings of the one-time simulation were excited with $9u_{fs}$ MMFs at the primary side and 0 MMF at the secondary side. The simulated flux was summed up in the same position along the y direction. Then, the summed magnetic flux was discretized by a step function as illustrated in Fig. 8, which can be expressed as:

$$\Phi = [\Phi_1, \Phi_2, \Phi_3, \Phi_4, \Phi_5, \Phi_6, \Phi_7, \Phi_8, \Phi_9, \Phi_{10}, \Phi_{11}, \Phi_{12}] \quad (2)$$

where, Φ_1, \dots, Φ_{12} are the simulated results obtained from the one-time simulation. As shown in Fig. 5, the total flux density of the corresponding part along the y axis can be calculated by:

$$\mathbf{B} = \Phi / A_c \quad (3)$$

where, A_c is the cross-sectional area seen from the x - z plane of the cores. The coefficient matrix \mathbf{M} can be acquired by dividing the total flux density along the y direction with the flux density in the corresponding blocks in the same column, as illustrated in Fig. 5.

According to Kirchhoff's Voltage Law, the magnetic reluctances in Fig. 8 can be obtained by substituting the simulated results of (2) into the proposed model. The expressions for calculating the magnetic reluctances in Fig. 8 are shown in the Appendix. In addition, the magnetic reluctance of the magnetic cores R_c in Fig. 8 can be calculated by:

$$R_c = \frac{l_c}{\mu_0 \mu_r A_c} \quad (4)$$

where, l_c is the length of the divided cores, μ_0 is the vacuum permeability and μ_r is the relative permeability of the cores.

Step 5: Calculating the core losses with different MMFs for optimization

After acquiring all of the parameters in Fig. 8, the magnetic flux density under different working conditions can be calculated by summing the results derived with the primary and secondary MMFs. Solving matrix \mathbf{A} in the Appendix is defined by analyzing the different looping circuits in Fig. 8. Thus, the flux density can be derived by:

$$\mathbf{B} = \mathbf{A}^{-1} \mathbf{U} / A_c \quad (5)$$

where, \mathbf{U} is the MMF matrix, which is defined by the divided MMF u_d as:

$$\mathbf{U} = [u_d, 2u_d, 2u_d, 2u_d, 2u_d, 2u_d, 2u_d, 2u_d, 2u_d, 0, 0, 0] \quad (6)$$

Hence, the flux density excited by the primary and secondary MMFs can be calculated by:

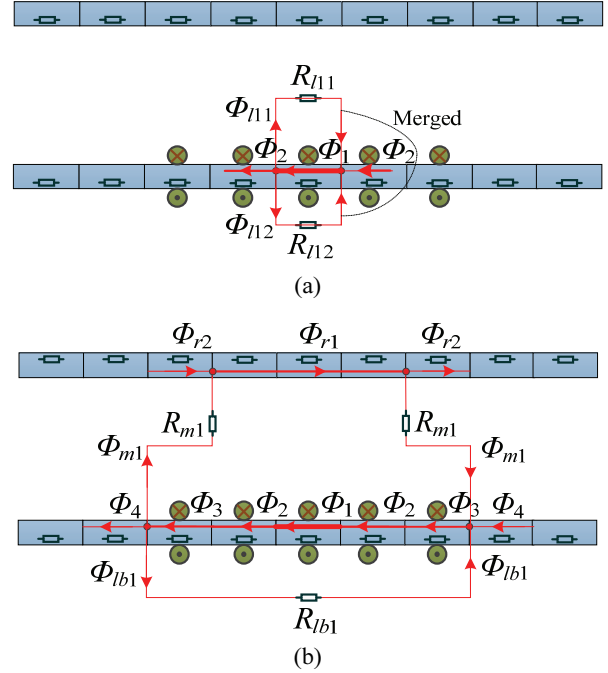


Fig. 7. Equivalent model of: (a) internal leakage flux density distribution; (b) mutual and other leakage flux density distributions.

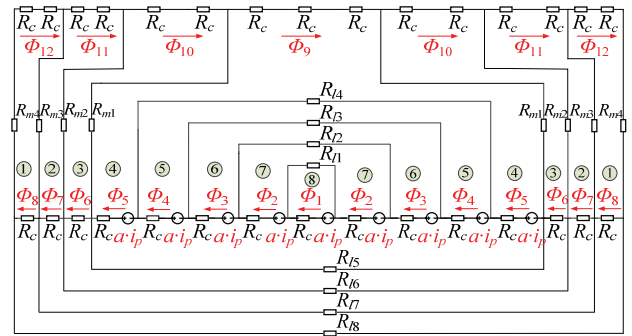


Fig. 8. Proposed magnetic-circuit model for a solenoid transformer.

$$\begin{cases} \mathbf{B}_p = \mathbf{A}^{-1} \mathbf{U}_p / A_c \\ \mathbf{B}_s = \mathbf{A}^{-1} \mathbf{U}_s / A_c \end{cases} \quad (7)$$

where, \mathbf{B}_p and \mathbf{B}_s are the flux density distributions by the primary and secondary excitations, and \mathbf{U}_p and \mathbf{U}_s are the MMF matrices of the primary and secondary windings, which can be expressed as:

$$\begin{cases} \mathbf{U}_p = [u_p, 2u_p, 2u_p, 2u_p, 2u_p, 2u_p, 2u_p, 2u_p, 2u_p, 0, 0, 0] \\ \mathbf{U}_s = [u_s, 2u_s, 2u_s, 2u_s, 2u_s, 2u_s, 2u_s, 2u_s, 2u_s, 0, 0, 0] \end{cases} \quad (8)$$

where, u_p and u_s are the divided MMFs of the primary and secondary excitation. By combining the results of \mathbf{B}_p and \mathbf{B}_s , the flux density distributions in the primary and secondary cores can be calculated as illustrated in Fig. 9.

Therefore, for cores under sinusoidal current excitation, the core losses P_c can be calculated by implementing a Steinmetz equation as:

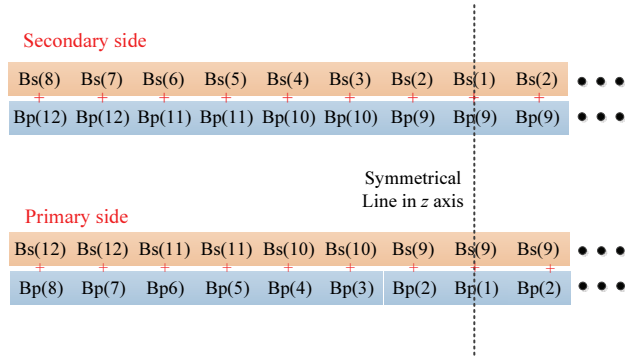


Fig. 9. Schematic diagram of the combination of the flux density with the primary and secondary MMFs.

$$P_c = \iint C_m f_s^\alpha B_m^\beta(x, y) dV \quad (9)$$

where, C_m , α and β are the parameters in the Steinmetz equation that can be obtained from the core datasheet, and V is the volume of the cores. By substituting (5)-(8) to (9), the loss distributions in the cores can be obtained.

Generally, the highest flux density crossing magnetic cores are designed under the saturated flux density of the selected ferrite to guide more flux to the secondary side [32]. Thus, ferrites usually work in the linear area of the B-H curve. As a result, the core losses can be summed by (9) in different divided cores with a Steinmetz Equation.

IV. MEASUREMENT OF THE WINDING RESISTANCE AND CALCULATION OF THE DEVICE LOSSES

A. The Measurement Method of the Winding Resistance

The winding losses are related to the excitation frequency in the coils. Thus, it is necessary to acquire the AC resistance of the windings to calculate the total losses. Most loss analysis methods [23] are not very applicable for the Litz windings in loosely coupled transformers since it is hard to model the bundles and the mutual influence of the inside strands. The simulation method is inaccurate for a 2D model but time-consuming for a 3D model with many small-diameter strands inside the Litz windings. Plus, the transformer structures of solenoid 'DD' or circular plates cannot be depicted precisely with simplified 2D models. Thus, it is hard to ensure precise calculation by FEM simulation tools. In [8], the AC resistance is acquired by measuring the Q values of the primary and secondary windings. However, the values are not precise since the equivalent resistance of the core losses are included in the test results according to the equivalent model of the transformers in Fig. 10. In [25], the authors proposed a simple method by analyzing the testing impedance of the differentially coupled transformer Z_{dif} and the cumulatively coupled transformer Z_{cum} , as illustrated in Fig. 10. R_{cp} and R_{cs} are the primary and secondary winding resistances, R_{core} is the core loss resistance, ω_s is the angular

frequency, n is the turn ratio of the secondary to the primary, L_{l1} and L_{l2} are the leakage inductances of the primary and secondary coils, and L_m is the excitation inductance. The inductance can be measured by the impedance analyzer. As presented in [25], by analyzing the equivalent circuit in Fig. 10 (a)-(b), the values of R_{core} can be derived as:

$$R_{core} = \frac{Z_{cum} - Z_{dif}}{4n} - j\omega_s L_m \quad (10)$$

Thus, with the derived core-loss resistance in (10), the resistance in the windings can be obtained by:

$$R_{cp} = \frac{\omega_s(L_{l1} + L_m)}{Q_p} - R_{core} \quad (11)$$

$$R_{cs} = \frac{\omega_s(L_{l2} + n^2 L_m)}{Q_s} - n^2 R_{core} \quad (12)$$

where, Q_p and Q_s are quality factors of the primary and secondary windings, which can be tested by an impedance analyzer. The winding resistances were measured at different frequencies from 1kHz to 100kHz, which covers most of the switching frequencies in EV applications.

B. The Device Losses of the System

As depicted in Fig. 11, the SP compensation topology is implemented in this study. An equivalent circuit of the transformers is illustrated with resonant capacitors (C_p and C_s) and equivalent resistors of the load R_{eq} . When L_o and C_o are connected with a high-frequency rectifier, R_{eq} can be calculated by:

$$R_{eq} = \frac{\pi^2}{8} R_o \quad (13)$$

Thus, the impedance of the secondary Z_s viewed from the primary side can be derived as:

$$Z_s = j\omega_s L_{l2} + R_{eq} // \left(\frac{1}{j\omega_s C_s} \right) + R_{cs} \quad (14)$$

The impedance from the input side of the primary side Z_p can be calculated by:

$$Z_p = (1/n)^2 Z_s // j\omega_s L_m + \frac{1}{j\omega_s C_p} + j\omega_s L_{l1} + R_{cp} \quad (15)$$

The loss resistance of the magnetic cores is neglected in the calculation since R_{core} has little influence on the current distribution. In order to minimize the input reactive power, the primary resonant capacitor C_p is chose to make the impedance Z_p resistance.

Both the core losses and the winding losses are determined by the primary current i_p and the secondary current i_s . i_p can be derived by:

$$i_p = \frac{u_p}{Z_p} \quad (16)$$

where, u_p is the fundamental component of the output voltage from the inverter circuit. As a result, the secondary resonant current can be calculated by:

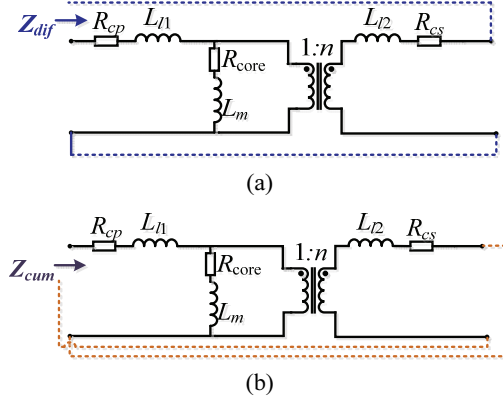


Fig. 10. Schematic diagram of the measurement method of the winding resistance.

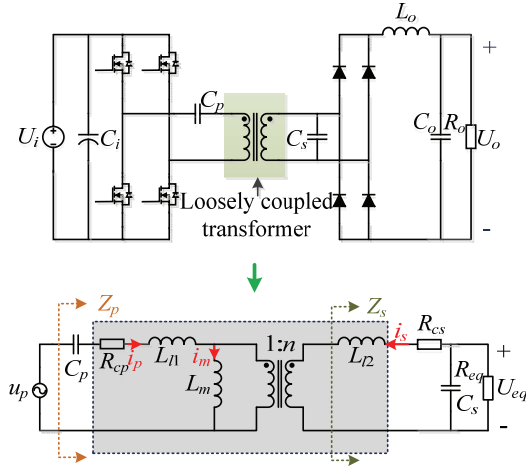


Fig. 11. Schematic diagram of the wireless charging system (top) and the equivalent circuit (bottom).

$$i_s = i_p \frac{j\omega_s L_m}{n((1/n)^2 Z_s + j\omega_s L_m)} \quad (17)$$

As a result, the voltage gain of the designed system can be derived with (10)-(17), as given by:

$$G_v = \frac{U_o}{U_i} = \left| \frac{0.818j\omega_s L_m R_{eq}}{Z_p n((1/n)^2 Z_s + j\omega_s L_m)(j\omega_s C_s R_{eq} + 1)} \right| \quad (18)$$

Normally, the switching devices operate in the ZVS condition, which leads to turn-on losses of the devices in the primary inverter being neglected. The on-state losses of the devices are determined by the conduction current, which can be calculated by:

$$P_{cond} = \frac{1}{2} I_{p_rms}^2 R_{DS(on)} \quad (19)$$

where, I_{p_rms} is the RMS value of the primary resonant current, and $R_{DS(on)}$ is the conduction resistance of the switching devices, which can be obtained from the datasheet of the devices. In addition, the switching losses are mainly generated during the turn-off process since the devices work on the ZVS condition. Thus, the turn-off losses P_{off} can be

calculated by [33]:

$$P_{off} = f_s \cdot E_{ref} \cdot \left(\frac{U_i}{U_{ref}} \right)^\alpha \left(\frac{I_{off}}{I_{ref}} \right)^\beta \quad (20)$$

where, f_s is the switching frequency, E_{ref} is the referenced energy loss during the turn-off process, U_i is the input voltage, I_{off} is the primary resonant current during the turn-off process, U_{ref} and I_{ref} are the referenced voltage and current from datasheets, and α and β are the exponential coefficients.

The losses of the high-frequency rectifier in the receiving circuit can be estimated by:

$$P_{diode} = \frac{1}{2} i_o u_F = \frac{1}{2} i_o \cdot (u_{ceo} + i_o \cdot R_{on}) \quad (21)$$

where, i_o is the output current, and u_F is the forward voltage of the diode, which is determined by the threshold voltage u_{ceo} and the on-state resistor R_{on} .

V. EXPERIMENTAL RESULTS AND DISCUSSIONS

A. Verification of the Proposed Loss Calculation Model

First, the magnetic-circuit model was validated by the FEM simulation tool. The primary current and secondary currents were calculated by (16)-(17) and then imported to the simulation tool. The magnetic cores are ferrites with a 2500 relative permeability. Table II gives the calculated magnetic reluctance in Fig. 8. Fig. 12 shows an experimental platform of the designed system. The specifications of the system, including the inductance and capacitors in the practical platform, are presented in Table III. The Litz wire consists of 400 strands with a 0.1mm diameter. When the input voltage is 163V, the calculated primary current is (8.41-0.60i)A and the secondary current is (5.99+25.99i)A. Under these operating conditions, the primary core losses and winding losses are 5W and 12.68W, while the secondary core losses and winding losses are 9.8W and 29.8W. Particularly, the switching frequency is 49.13kHz, which was set according to the measured C_s and L_2 . As a result, the magnetic flux density in different positions was calculated and compared with the simulation data as pictured in Fig. 13. It is worth noting that the derivations of the simulated and calculated results are so small that they have little impact on the core loss calculation. In addition, with different primary and secondary current and turns, the flux density distribution can be obtained by the proposed model in a short time.

The experiment is divided into three stages. Firstly, the parameters of the transformers including the inductance and resistance were measured by an Agilent E4980A LCR meter [24]. After that, the secondary and primary capacitors were selected and the switching frequency was determined. Then, the inductive charging system operated at a different input voltage. Meters are then used to test the input and output current and voltage to get the power losses of the system. The specifications of the system were imported to the calculated

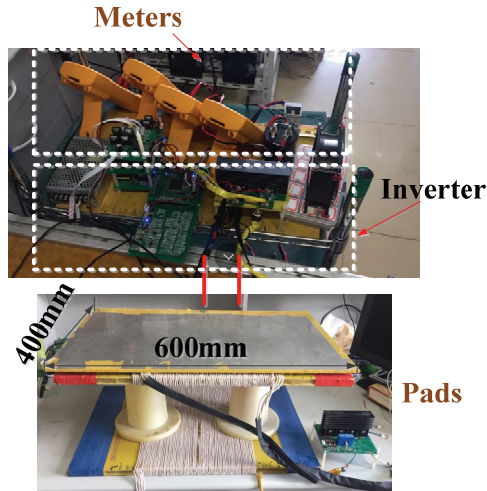


Fig. 12. Platform of the designed systems

TABLE II

MAGNETIC RELUCTANCE IN FIGURE 7 (UNIT: H)

R_{l1}	21.37	R_{l5}	28.81	R_{m1}	45.76
R_{l2}	20.86	R_{l6}	53.92	R_{m2}	21.61
R_{l3}	19.42	R_{l7}	55.88	R_{m3}	17.47
R_{l4}	15.29	R_{l8}	24.38	R_{m4}	23.76

TABLE III

SPECIFICATIONS OF THE SYSTEM

Primary inductance L_1	207.8 μ H
Secondary inductance L_2	56.4 μ H
Coupling Coefficient k	0.266
Primary capacitor C_p	55.3nF
Secondary capacitor C_s	245.6nF
Load resistance R_o	58.6 Ω
Primary winding turns	18
Secondary winding turns	8
Switching devices	IPW65R019C7 (700V 62A)
Diodes	IDW30G65C5 (650V 30A)
Size of magnetic cores	60mm:35mm:12mm ($\mu_r = 2500$)
Resonant capacitor	DTR1200 (3000V)

model. Fig. 15 shows test waveforms of the system including the primary current i_p , secondary current i_s and output voltage of the inverter u_p . It can be found that the ZVS condition was realized and that there is not much of a voltage spike in the waveforms. In addition, the experimental and calculated power losses were pictured in Fig. 16(a). It can be seen that

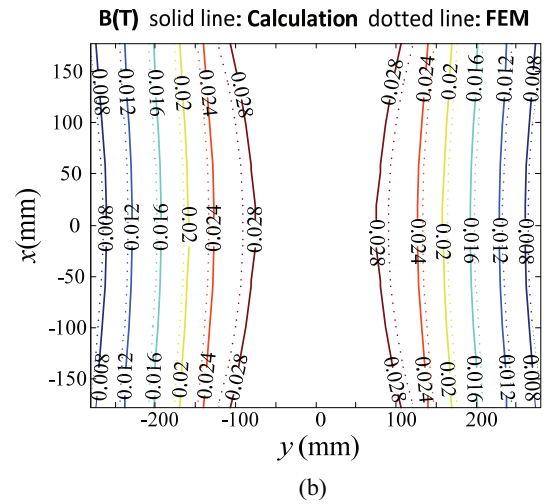
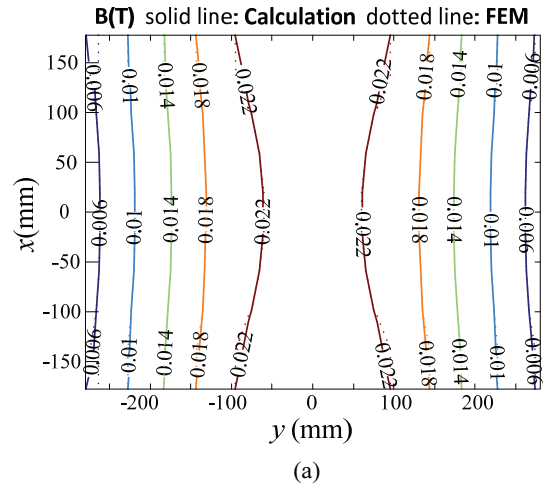


Fig. 13. Results of the calculated and FEM simulated flux density distribution in the cores of the: (a) primary side; (b) secondary side.

the calculated results by the proposed model are consistent with the measured results. The largest deviation is less than 5%, which partly comes from the imprecise parameters in (9) of the core losses and deviations in the manufacturing and simulation models. The core losses from the experiment and calculation were compared, as depicted in Fig. 16(b). Since it is hard to directly obtain the losses inside magnetic cores, the experimental core losses were obtained by subtracting the measured total losses with the measured winding losses by using a LCR meter, the switching device losses and the diode losses by integrating the voltage and current waveforms with a HDO4034 oscilloscope. The small deviation in the results verifies the proposed magnetic-circuit model. Fig. 16(c) shows the loss distributions of the system with different input voltages according to the calculated results. The winding losses and core losses of the primary and secondary account for the bulk of the total losses. Moreover, the losses in the switching devices and diodes makes up a small proportion of the total losses and increase slowly.

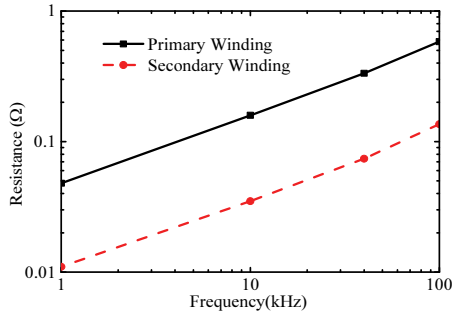


Fig. 14. Measured winding resistance of the primary and secondary.

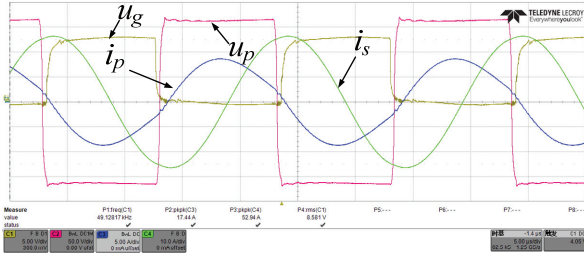


Fig. 15. Test waveforms of the system.

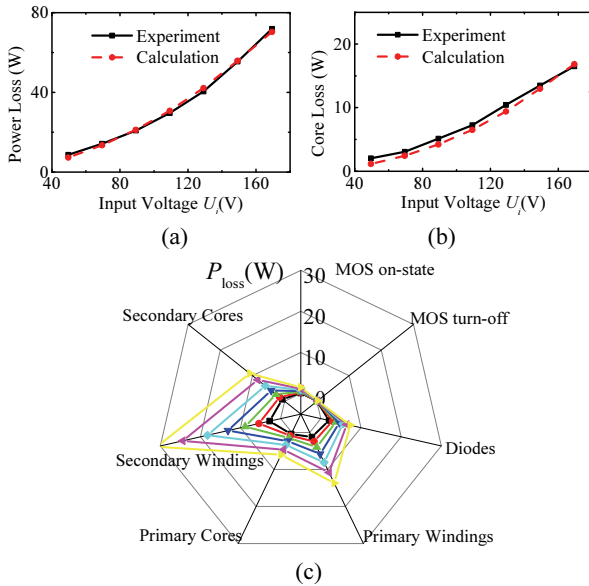


Fig. 16. Graphs showing: (a) comparison of the calculated and measured results of the total power loss; (b) comparison of the calculated and measured results of the core loss; (c) loss distributions with different input voltages.

B. Discussions of Efficiency Optimization

1) Optimized Switching Frequency

The switching frequency is an important parameter that plays an essential role in the switching losses, core losses and winding losses. Thus, it is significant to give the quantity relations between the switching frequency and the system efficiency. In this paper, the discussion about the switching frequencies is separated into two scales. These scales are the

large scale and the local scale. The large scale is defined from 10kHz to 100kHz, which covers most of the switching frequencies in inductive charging systems. For the local scale, the capacitors are fixed to find a higher-efficiency frequency at a small scale around a predesigned frequency. Specifically, the input voltage is 200V and the load of the system is determined to be 58.6Ω.

On the one hand, the increased frequency raises the switching losses, but has little influence on the diode losses of the rectifier in the secondary side. In addition, increasing the frequency can lead to an increase of the AC resistance of the windings. On the other hand, the primary and secondary resonant current is influenced by the switching frequency since the frequency changes the impedance in Fig. 11. Thus, efficiency with different switching frequencies is investigated and depicted in Fig. 17. The scale of the switching frequency is set from 10kHz to 100kHz. It can be concluded that efficiency rises with the switching frequency. However, the increasing slope decreases and becomes smooth when the frequency outstrips 40kHz. Another issue that should be considered is the variation of the voltage gain with increased frequencies. The results in Fig. 17 indicates that the gain G_v varies less than 1.5%, which is due to changes of the winding resistance. In order to obtain a deeper understanding of the features, the variations for each of the partial losses are pictured in Fig. 18. P_{MOS} is the losses in the switching devices including the on-state losses and turn-off losses, P_{Diode} is the losses in the diodes, P_{p_copper} and P_{s_copper} are the copper losses in the primary and secondary windings, P_{p_core} and P_{s_core} are the core losses in the primary and secondary cores, and P_{tot} is the total losses of the whole system. As can be seen from Fig. 18, the losses of the switching devices and diodes decrease slightly, due in large part to the smaller voltage gain when the frequency becomes larger. The coppers losses become smaller since the secondary current decrease dramatically, as can be seen from the calculated results in Fig. 19. According to (9), the core losses are determined by two factors: the frequency and the flux density, which is induced by currents in the windings. When the switching frequency increases, the total core losses in Fig. 18 decrease since the resonant currents decrease notably, as shown in Fig. 19. Then the total core losses increase because the frequency becomes larger and the change in the currents becomes much smaller. Since the copper losses form the majority of the total losses, the losses decreases when the copper losses become smaller with higher frequencies. However, when the switching frequencies get higher, the core losses become larger after the first become smaller.

When the scale of the frequency is determined according to the curves in Fig. 17, the switching frequency of the system is usually precisely designed by calculating the oscillating frequency of the measured secondary resonant capacitor C_s and secondary self-inductance L_2 , since the output power is

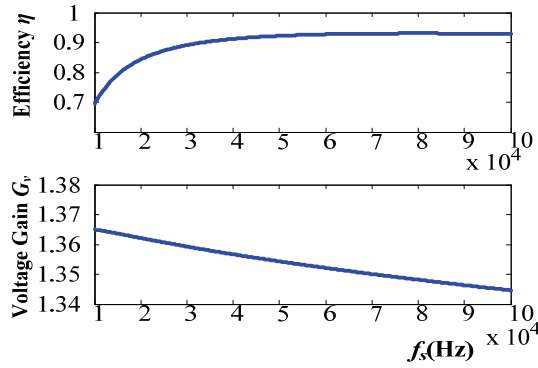


Fig. 17. Efficiency and voltage gain versus different switching frequencies.

highest when the primary resonant current is fixed [34]. In the designed system, the resonant designed frequency f_{s_res} is 49.13kHz with C_s (245.6nF) and L_2 (56.4μH). However, for topologies with primary or secondary DC/DC converters, the primary resonant current is unnecessarily controlled to be consistent. Therefore, the frequencies varying around the designed frequency are investigated as shown in Fig. 20. When compared with the calculation of large-scale frequencies, the system parameters including the inductance and capacitance are fixed. According to the calculated results, a higher-efficiency frequency, which differs from the resonant frequency, is detected as f_{s_opt} . This frequency is about 1.8kHz lower than the frequency f_{s_res} , while the efficiency is 0.5% higher than the predesigned one. In addition, the voltage gain G_v becomes lowest when the frequency approaches f_{s_res} , which means a higher power transfer can be obtained with the frequency f_{s_opt} . The condition of realizing ZVS is also a restriction on the system design. It can be found that the phase of the input impedance Z_p is above zero and greater than the predesigned phase. Furthermore, loss variations with different frequencies are depicted in Fig. 21. The losses of the switching devices and the rectifier changes are lowest when the phase of Z_p turns to zero. However, the frequency is different from the frequencies when obtaining the minimum losses of the windings, cores and total system. Thus, in order to achieve the highest efficiency, each partial loss and the voltage gain should be integrally analyzed.

However, the above system is not desirable because the frequency bifurcation makes the variable frequency control harder [35]. Thus, a higher frequency of about 80kHz is designed with the same analysis method. The predesigned frequency is 77.33kHz when the secondary capacitor C_s is 98.9nF. The higher-efficiency frequency is 74.00kHz on the basis of the proposed loss calculation model. Particularly, the impedance Z_p rises continuously with the switching frequency, which results in stable systems with variable frequency control [35]. The results in Fig. 22 indicate that the efficiency can be increased by 0.3%.

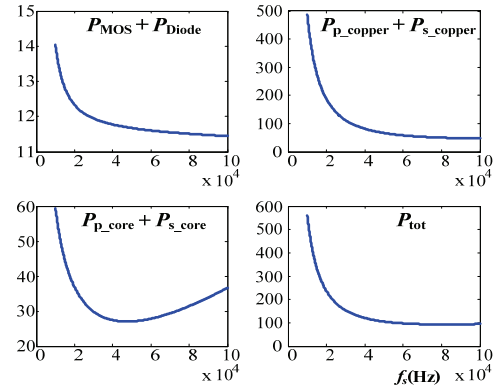


Fig. 18. Loss distributions versus different switching frequencies on a large scale.

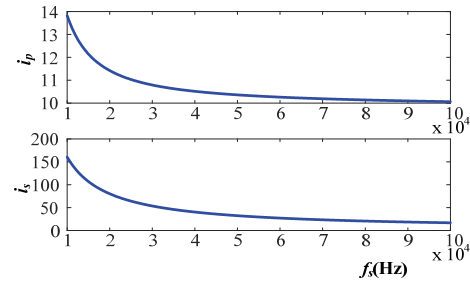


Fig. 19. Primary and secondary currents versus different switching frequencies.

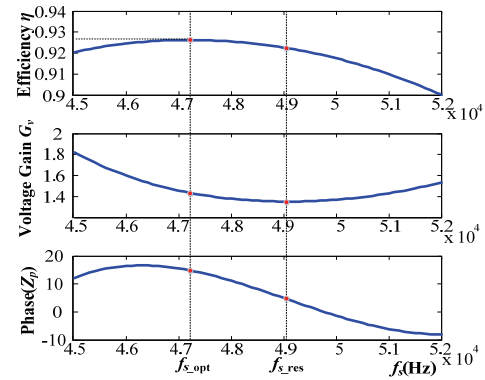


Fig. 20. Efficiency, voltage gain and phase of Z_p versus different switching frequencies on a small scale.

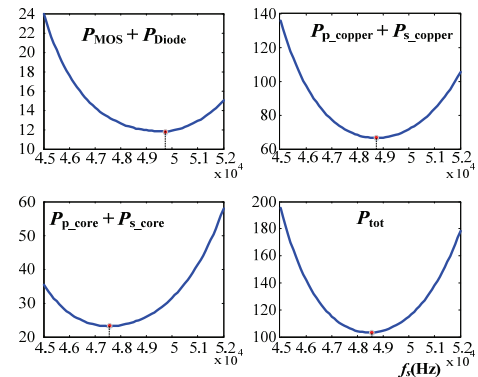


Fig. 21. Loss distributions versus different switching frequencies on a small scale.

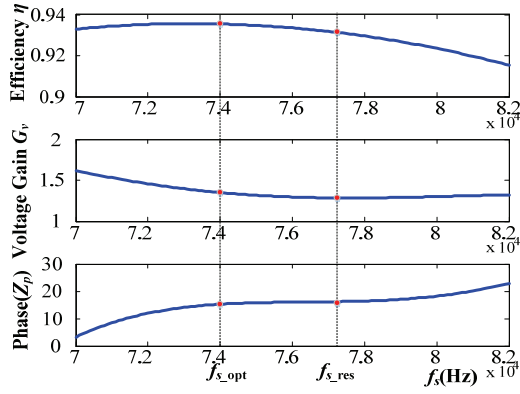


Fig. 22. Efficiency, voltage gain and phase of Z_p versus different switching frequencies on a local scale.

2) Optimized Combinations of Coil Turns

In addition to the switching frequency, the turns of the primary and secondary are also key elements that determine the efficiency of the system. Except for the turn ratios, the efficiency is also influenced by the turns since the winding resistance and magnetic flux density vary with different turns. Meanwhile, the voltage gain should be met to receive enough output power for the secondary side. The voltage gain is set between 1 and 1.5 for the designed systems, which is suitable for EV charging applications [36]. Fig. 23 gives the calculated results of different primary and secondary turns. The range of the primary and secondary turns are limited to less than 30 by considering the diameter of the windings and the dimensions of the plate. The efficiency can reach as high as 92.5% with a 50kHz switching frequency when the turns of the secondary changes from 9 to 10 and the primary turns are more than 18. In order to satisfy the design of the voltage gain, a target area is defined as the turn that combines achieving the highest efficiency and a reasonable voltage gain. When the switching frequency changes from 50kHz to 80kHz, the target area moves to smaller primary and secondary turns as shown in Fig. 23(b). The primary turns are limited from 14 to 22 and the secondary turns is from 7 to 8. For predesigned system with 18 primary turns and 8 secondary turns, 80kHz is more suitable as the switching frequency of a system located in the target area in Fig. 23(b).

In order to illustrate variations of the efficiency versus different primary and secondary turns, the proportions of the copper and core losses in the total input power P_{in} are depicted with different turn combinations, as shown in Fig. 24. As can be seen from Fig. 24, the primary copper losses and core losses decrease while the secondary copper and core losses increase, when the secondary turn becomes larger. In addition, the primary turn has an influence on the change of the loss distribution. The reason for the efficiency variations with different turn combinations is that the impedance of the system is changed with different primary and secondary turns, which results in changes in the primary and secondary current.

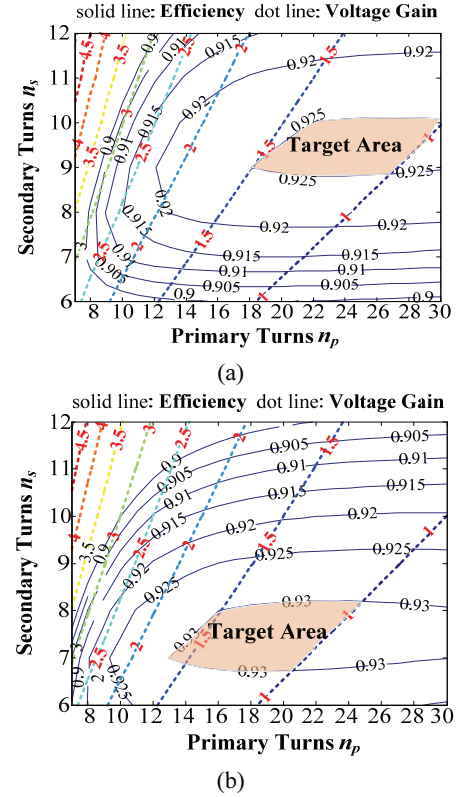


Fig. 23. Efficiency and voltage gain versus different primary turns n_p and secondary turns n_s at: (a) 50kHz; (b) 80kHz.

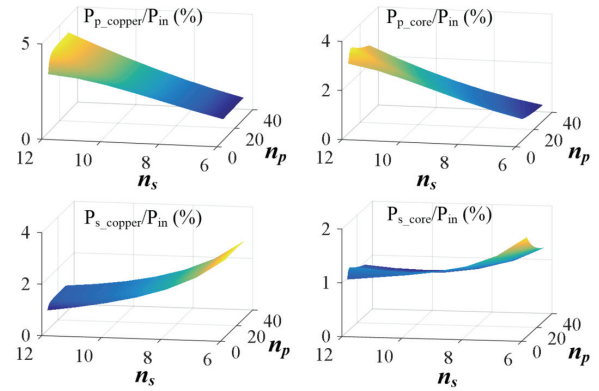


Fig. 24. Losses distribution in a loosely coupled transformer versus different primary turns n_p and secondary turns n_s at a switching frequency of 80kHz.

3) Experiment Verification

A platform was established to validate the optimized process. First, the efficiency was tested under 49.1kHz with different input voltages. Then, the switching frequency was changed to different frequencies lower than 49.1kHz. After that, the secondary capacitor C_s was replaced by 98.4nF and the primary capacitor C_p was substituted by 23.5nF. Accordingly, the efficiency was tested under 77.3 kHz and a relatively lower frequency. Figs. 25(a)-(b) give the test efficiencies of different switching frequencies with variable input voltages. By comparing the efficiencies in Fig. 25(a) and Fig. 25(b),

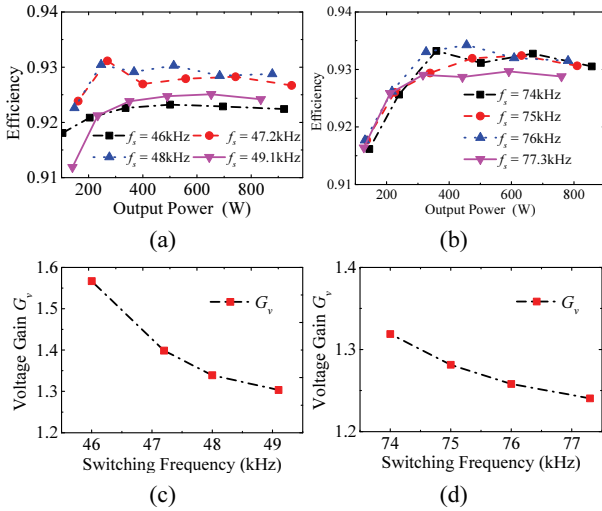


Fig. 25. Measured efficiency versus different switching frequencies at around: (a) 50kHz (b) 80kHz; along with (c) and (d) the corresponding voltage gain versus different frequencies.

the results indicate that a higher switching frequency leads to a greater efficiency. In addition, the curves in Fig. 25(a) or Fig. 25(b) reveal that the efficiency with f_{s_opt} is higher than that with f_{s_res} , which validates the analysis in this chapter. For the system design, the frequency should be determined at a large scale and then f_{s_opt} rather than f_{s_res} at a small scale. Another issue that should be considered is the voltage gain G_v at different switching frequencies. As can be seen in Fig. 25(c)-(d), the voltage gain decreases when the switching

frequencies change from 50kHz to 80kHz. The gain is also a limitation for designing the switching frequencies of systems.

The above optimization process was carried out with a 200cm air gap between the primary and secondary pads with dimensions of 600mm×400mm. For different air gaps and pad sizes, the proposed method is still applicable since only several FEM simulations need to be done and the corresponding optimization can be implemented to find the proper switching frequency and turn combinations as shown in Section V.

VI. CONCLUSIONS

In this paper, a loss calculation method for the loosely coupled transformers in inductive power systems is proposed with a novel magnetic-circuit model, which is derived according to the flux distribution of the solenoid structure. The parameters of the magnetic-circuit model can be obtained by a one-time FEM simulation, which leads to a fast and accurate optimization process. Meanwhile, the winding resistance varying with the frequency is achieved by a practical method. Experimental results obtained with a test platform verify that the frequency was detected and analyzed in detail. Sweeping maps with different primary and secondary turns were also provided to give a more convenient optimization process. The obtained experimental results show great agreement with the presented optimization.

APPENDIX

$$\begin{aligned}
 R_{l1} &= (u_{fs} - B_1 R_c) / (B_1 - B_2) \\
 R_{l2} &= (3u_{fs} - B_1 R_c - 2B_2 R_c) / (B_2 - B_3) \\
 R_{l3} &= (5u_{fs} - B_1 R_c - 2B_2 R_c - 2B_3 R_c) / (B_3 - B_4) \\
 R_{l4} &= (7u_{fs} - B_1 R_c - 2B_2 R_c - 2B_3 R_c - 2B_4 R_c) / (B_4 - B_5) \\
 R_{l5} &= (9u_{fs} - B_1 R_c - 2B_2 R_c - 2B_3 R_c - 2B_4 R_c - 2B_5 R_c) / (B_5 - B_6 - B_9 + B_{10}) \\
 R_{l6} &= (9u_{fs} - B_1 R_c - 2B_2 R_c - 2B_3 R_c - 2B_4 R_c - 2B_5 R_c - 2B_6 R_c) / (B_6 - B_7 - B_{10} + B_{11}) \\
 R_{l7} &= (9u_{fs} - B_1 R_c - 2B_2 R_c - 2B_3 R_c - 2B_4 R_c - 2B_5 R_c - 2B_6 R_c - 2B_7 R_c) / (B_7 - B_8 - B_{11} + B_{12}) \\
 R_{l8} &= (9u_{fs} - B_1 R_c - 2B_2 R_c - 2B_3 R_c - 2B_4 R_c - 2B_5 R_c - 2B_6 R_c - 2B_7 R_c - 2B_8 R_c) / (B_8 - B_{12}) \\
 R_{m1} &= (9u_{fs} - B_1 R_c - 2B_2 R_c - 2B_3 R_c - 2B_4 R_c - 2B_5 R_c - 3B_9 R_c) / (2B_9 - 2B_{10}) \\
 R_{m2} &= (9u_{fs} - B_1 R_c - 2B_2 R_c - 2B_3 R_c - 2B_4 R_c - 2B_5 R_c - 2B_6 R_c - 3B_9 R_c - 4B_{10} R_c) / (2B_{10} - 2B_{11}) \\
 R_{m3} &= (9u_{fs} - B_1 R_c - 2B_2 R_c - 2B_3 R_c - 2B_4 R_c - 2B_5 R_c - 2B_6 R_c - 3B_9 R_c - 4B_{10} R_c - 4B_{11} R_c) / (2B_{11} - 2B_{12}) \\
 R_{m4} &= (9u_{fs} - B_1 R_c - 2B_2 R_c - 2B_3 R_c - 2B_4 R_c - 2B_5 R_c - 2B_6 R_c - 3B_9 R_c - 4B_{10} R_c - 4B_{11} R_c - 4B_{12} R_c) / (2B_{12})
 \end{aligned}$$

$$\mathbf{A} = \begin{bmatrix}
 R_c + R_{l1} & -R_{l1} & 0 & 0 & 0 & 0 & 0 & 0 & 0 & 0 & 0 & 0 \\
 -R_{l1} & 2R_c + R_{l1} + R_{l2} & -R_{l2} & 0 & 0 & 0 & 0 & 0 & 0 & 0 & 0 & 0 \\
 0 & -R_{l2} & 2R_c + R_{l2} + R_{l3} & -R_{l3} & 0 & 0 & 0 & 0 & 0 & 0 & 0 & 0 \\
 0 & 0 & -R_{l3} & 2R_c + R_{l3} + R_{l4} & -R_{l4} & 0 & 0 & 0 & 0 & 0 & 0 & 0 \\
 0 & 0 & 0 & -R_{l4} & 2R_c + R_{l4} + R_{l5} & -R_{l5} & 0 & 0 & -R_{l5} & R_{l5} & 0 & 0 \\
 0 & 0 & 0 & -R_{l4} & 2R_c + R_{l4} & 2R_c + R_{l6} & -R_{l6} & 0 & 0 & -R_{l6} & R_{l6} & 0 \\
 0 & 0 & 0 & -R_{l4} & 2R_c + R_{l4} & 2R_c & 2R_c + R_{l7} & -R_{l7} & 0 & 0 & -R_{l7} & R_{l7} \\
 0 & 0 & 0 & -R_{l4} & 2R_c + R_{l4} & 2R_c & 2R_c & 2R_c + R_{l8} & 0 & 0 & 0 & -R_{l8} \\
 0 & 0 & 0 & -R_{l4} & 2R_c + R_{l4} & 0 & 0 & 0 & 2R_{m1} + 3R_c & -2R_{m1} & 0 & 0 \\
 0 & 0 & 0 & 0 & 0 & R_c & 0 & 0 & -R_{m1} & 2R_c + R_{m1} + R_{m2} & -R_{m2} & 0 \\
 0 & 0 & 0 & 0 & 0 & 0 & R_c & 0 & 0 & -R_{m2} & 2R_c + R_{m2} + R_{m3} & -R_{m3} \\
 0 & 0 & 0 & 0 & 0 & 0 & 0 & R_c & 0 & 0 & -R_{m3} & 2R_c + R_{m3} + R_{m4}
 \end{bmatrix}$$

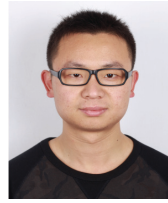
ACKNOWLEDGMENT

This work was supported by the National Natural Science Foundation of China under grant no. 51577171.

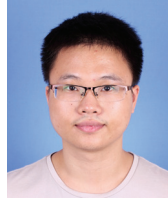
REFERENCES

- [1] G. B. Joung and B. H. Cho, "An energy transmission system for an artificial heart using leakage inductance compensation of transcutaneous transformer," *IEEE Trans. Power Electron.*, Vol. 13, No. 6, pp. 1013-1022, Nov 1998.
- [2] D. Roberson, A. Chu, A. Sabitov, and G. A. Covic, "High powered IPT stage lighting controller," in *Proc. IEEE Int. Symp. Ind. Electron.*, pp. 1974-1979, 2011.
- [3] K. I. Woo, H. S. Park, Y. H. Choo, and K. H. Kim, "Contactless energy transmission system for linear servo motor" *IEEE Trans. Magn.*, Vol. 41, No. 5, pp. 1596-1599, May 2005.
- [4] A. W. Green and J. T. Boys, "10kHz inductively coupled power transfer-concept and control" in *Proc. 5th Int. Conf. Power Electron. Variable-speed Drives*, pp. 694-699, 1994.
- [5] M. Eghtesadi, "Inductive power transfer to an electric vehicle-analytical model" in *Proc. 40th Veh. Technol. Conf.*, pp. 100-104., 1990.
- [6] G. A. Covic, J. T. Boys, M. L. G. Kissin, and H. G. Lu, "A three-phase inductive power transfer system for roadway-powered vehicles," *IEEE Trans. Ind. Electron.*, Vol. 54, No. 6, pp. 3370-3378, Dec. 2007.
- [7] J. Huh, S. W. Lee, W. Y. Lee, G. H. Cho, and C. T. Rim, "Narrow-width inductive power transfer system for online electrical vehicles," *IEEE Trans. Power Electron.*, Vol. 26, No. 12, pp. 2666-2679, Dec. 2011.
- [8] M. Budhia, G. A. Covic, and J. T. Boys, "Design and optimization of circular magnetic structures for lumped inductive power transfer systems," *IEEE Trans. Power Electron.*, Vol. 26, No. 11, pp. 3096-3108, Nov. 2011.
- [9] J. Kim, S. Kong, H. Kim, I. S. Suh, N. P. Suh, D. H. Cho, and S. Ahn, "Coil design and shielding methods for a magnetic resonant wireless power transfer system," *Proc. IEEE*, Vol. 101, No. 6, pp. 1332-1342, Jun. 2013.
- [10] M. Budhia, J. T. Boys, G. A. Covic, and C. Y. Huang, "Development of a single-sided flux magnetic coupler for electric vehicle IPT charging systems," *IEEE Trans. Ind. Electron.*, Vol. 60, No. 1, pp. 318-328, Jan 2013.
- [11] M. Budhia, G. A. Covic, and J. T. Boys, "A new IPT magnetic coupler for electric vehicle charging systems," in *Proc. 36th Annu. Conf. IEEE Ind. Electron. Soc.*, (IECON'10), pp. 2487-2492, 2010.
- [12] Y. Nagatsuka, N. Ehara, Y. Kaneko, S. Abe, and T. Yasuda, "Compact contactless power transfer system for electric vehicles," in *Proc. Int. Power Electron. Conf.*, Sapporo, pp. 807-813, 2010.
- [13] Y. Xiong, S. Sun, H. Jia, P. Shea, and Z. J. Shen, "New physical insights on power MOSFET switching losses," *IEEE Trans. Power Electron.*, Vol. 24, No. 2, pp. 525-531, Feb. 2009.
- [14] X. Nan and R. Sullivan, "An equivalent complex permeability model for Litz-wire windings," *IEEE Trans. Ind. Appl.*, Vol. 45, No. 2, pp.854-860, Mar/Apr 2009.
- [15] J. Muhlethaler, J. Biela, J. W. Walter, and A. Ecklebe, "Improved core-loss calculation for magnetic components employed in power electronic systems," *IEEE Trans. Power Electron.*, Vol. 27, No. 2, pp. 964-973, Feb. 2012.
- [16] C. P. Steinmetz, "On the law of hysteresis," *Proc. IEEE*, Vol. 72, No. 2, pp. 197-221, Feb. 1984.
- [17] S. Wang and D. G. Dorrell, "Loss analysis of circular wireless EV charging coupler," *IEEE Trans. Magn.*, Vol. 50, No. 11, Article No. 8402104, Nov. 2014.
- [18] Z. Cheng, Y. Lei, K. Song, and C. Zhu, "Design and loss analysis of loosely coupled transformer for an underwater high-power inductive power transfer system," *IEEE Trans. Magn.*, Vol. 51, No. 7, Article No. 8401110, Jul. 2015.
- [19] J. Sibue, G. Kwimang, J. Ferrieux, G. Meunier, J. Roudet, and R. Periot, "A global study of a contactless energy transfer system analytical design, virtual prototyping, and experimental validation," *IEEE Trans. Power Electron.*, Vol. 28, No. 10, pp. 4690-4699, Oct. 2013.
- [20] A. J. Moradewicz and M. P. Kazmierkowski, "Contactless energy transfer system with FPGA-controlled resonant converter," *IEEE Trans. Power Electron.*, Vol. 57, No. 9, pp. 3181-3190, Sep. 2010.
- [21] W. Zhang, Q. Chen, S. C. Wong, C. K. Tse, and X. Ruan, "A novel transformer for contactless energy transmission systems," in *Proc. IEEE Energy Conver. Congr. Expo.*, 2009, Vol. 1-6, pp. 2679-2685.
- [22] J. A. Ferreira, "Improved analytical modeling of conductive losses in magnetic components," *IEEE Trans. Power Electron.*, Vol. 9, No. 1, pp. 127-131, Jan 1994.
- [23] E. L. Barrios, A. Ursua, L. Marroyo, and P. Sanchis, "Analytical design methodology for Litz-wired high-frequency power transformers," *IEEE Trans. Ind. Electron.*, Vol. 62, No. 4, pp. 2103-2113, Apr 2015.
- [24] Y. Han, W. Eberle, and Y. Liu, "A practical copper loss measurement method for the planar transformer in high-frequency switching converters," *IEEE Trans. Ind. Electron.*, Vol. 54, No. 4, pp. 2276-2287, Aug 2007.
- [25] J. G. Hayes, D. Cashman, M. G. Egan, T. Donnell, and N. Wang, "Comparison of test methods for characterization of high-leakage two-winding transformers," *IEEE Trans. Ind. Appl.*, Vol. 45, No. 5, pp.1729-1741, Sep/Oct 2009.
- [26] H. Rossmanith, M. Doebroenti, M. Albach, and D. Exner, "Measurement and characterization of high frequency losses in nonideal Litz wires," *IEEE Trans. Power Electron.*, Vol. 26, No. 11, pp. 3386-3394, Nov 2011.
- [27] Z. N. Low, R. A. Chinga, R. Tseng, and J. Lin, "Design and test of a high-power high-efficiency loosely coupled planar wireless power transfer system," *IEEE Trans. Ind. Electron.*, Vol. 56, No. 5, pp. 1801-1812, May 2009.
- [28] N. Liu and T. G. Habetler, "Design of a universal inductive charger for multiple electric vehicle models," *IEEE Trans. Power Electron.*, Vol. 30, No. 11, pp. 6378-6390, Nov 2015.
- [29] S. Valtchev, B. Borges, K. Brandisky, and J. B. Klaassens, "Resonant contractless energy transfer with improved efficiency," *IEEE Trans. Power Electron.*, Vol. 24, No. 3, pp. 685-699, Mar. 2009.

- [30] H. H. Wu, A. Gilchrist, K. D. Sealy, and D. Bronson, "A high efficiency 5 kW inductive charger for EVs using dual side control," *IEEE Trans. Ind. Informat.*, Vol. 8, No. 3, pp. 585–595, Jan. 2012.
- [31] W. Zhang, S. Wong, C. Tse, and Q. Chen, "Design for efficiency optimization and voltage controllability of series-series compensated inductive power transfer systems," *IEEE Trans. Power Electron.*, Vol. 29, No. 1, pp. 191–200, Jan. 2014.
- [32] R. W. Erickson and D. Maksimovic, *Fundamentals of Power Electronics*, 2nd ed. Norwell, MA: Kluwer, chap. 13, 2001.
- [33] A. Wintrich, U. Nicolai, W. Tursky, and T. Reimann, *Application Manual Power Semiconductors*. Germany: SEMIKRON International GmbH, 2015.
- [34] W. Zhang, S. C. Wong, C. K. Tse, and Q. H. Chen, "Analysis and comparison of secondary series- and parallel-compensated inductive power transfer systems operating for optimal efficiency and load-independent voltage-transfer ratio," *IEEE Trans. Power Electron.*, Vol. 29, No. 6, pp. 2979–2990, Jun. 2014.
- [35] C. Wang, O. H. Stielau, and G. A. Covic, "Design considerations for a contactless electric vehicle battery charger," *IEEE Trans. Ind. Electron.*, Vol. 52, No. 5, pp. 1308–1314, Oct 2005.
- [36] M. Yilmaz and P. T. Krein, "Review of battery charger topologies, charging power levels, and infrastructure for plug-in electric and hybrid vehicles," *IEEE Trans. Power. Electron.*, Vol. 28, No. 5, pp. 2151–2169, May 2013.



Yunyu Tang was born in Jiangsu, China, in 1990. He received his B.S. degree in Electrical Engineering from Zhejiang University, Hangzhou, China, in 2013, where he is presently working towards his Ph.D. degree. His current research interests include IGBT modules and wireless power transfer systems.



Fan Zhu was born in Zhejiang, China, in 1989. He received his B.S. degree in Electrical Engineering from Zhejiang University, Hangzhou, China, in 2012, where he is presently working towards his Ph.D. degree. His current research interests include wireless power transfer systems.



Hao Ma (M'99) received his B.S., M.S. and Ph.D. degrees in Electrical Engineering from Zhejiang University, Hangzhou, China, in 1991, 1994 and 1997, respectively. He is presently working as a Professor in the College of Electrical Engineering, Zhejiang University. His current research interests include advanced control in power electronics, fault diagnosis of power electronic circuits and systems, and the application of power electronics.